



In-vivo imaging of the palisades of Vogt and the limbal crypts with sub-micrometer axial resolution optical coherence tomography

KOSTADINKA BIZHEVA,^{1,2,3,*} BINGYAO TAN,¹ BENJAMIN MACLELLAN,¹ ZOHREH HOSSEINAE,³ ERIK MASON,¹ DENISE HILEETO,² AND LUIGINA SORBARA²

¹Department of Physics and Astronomy, University of Waterloo, Waterloo, ON, N2L 3G1, Canada

²School of Optometry and Vision Sciences, University of Waterloo, Waterloo, ON, N2L 3G1, Canada

³Systems Design Engineering Department, University of Waterloo, Waterloo, ON, N2L 3G1, Canada

*kbizheva@uwaterloo.ca

Abstract: A research-grade OCT system was used to image *in-vivo* and without contact with the tissue, the cellular structure and microvasculature of the healthy human corneo-scleral limbus. The OCT system provided 0.95 μm axial and 4 μm (2 μm) lateral resolution in biological tissue depending on the magnification of the imaging objective. Cross-sectional OCT images acquired tangentially from the inferior limbus showed reflective, loop-like features that correspond to the fibrous folds of the palisades of Vogt (POV). The high OCT resolution allowed for visualization of individual cells inside the limbal crypts, capillaries extending from the inside of the POV's fibrous folds and connecting to a lateral grid of micro-vessels located in the connective tissue directly below the POV, as well as reflections from individual red blood cells inside the capillaries. Difference in the reflective properties of the POV was observed among subjects of various pigmentation levels of the POV. Morphological features observed in the high resolution OCT images correlated well with histology. The ability to visualize the limbal morphology and microvasculature *in-vivo* at cellular level can aid the diagnostics and treatment of limbal stem cell dysfunction and dystrophies.

© 2017 Optical Society of America

OCIS codes: (170.4500) Optical coherence tomography; (170.3880) Medical and biological imaging; (170.3890) Medical optics instrumentation; (170.0110) Imaging systems.

References and links

1. M.J. Hogan, J. A. Alvarado, *Histology of the Human Eye: An Atlas and Textbook* (1971).
2. E. M. Van Buskirk, "The anatomy of the limbus," *Eye (Lond.)* **3**(2), 101–108 (1989).
3. J. G. Lawrenson and G. L. Ruskell, "The structure of corpuscular nerve endings in the limbal conjunctiva of the human eye," *J. Anat.* **177**, 75–84 (1991).
4. P. A. Meyer, "The circulation of the human limbus," *Eye (Lond.)* **3**(Pt 2), 121–127 (1989).
5. E. B. Papas, "The limbal vasculature," *Cont. Lens Anterior Eye* **26**(2), 71–76 (2003).
6. H. S. Dua, A. Azuara-Blanco, and E. Fisher, "Limbal Stem Cells of the Corneal Epithelium," *Surv. Ophthalmol.* **44**(5), 415–425 (2000).
7. H. S. Dua, V. A. Shanmuganathan, A. O. Powell-Richards, P. J. Tighe, and A. Joseph, "Limbal epithelial crypts: a novel anatomical structure and a putative limbal stem cell niche," *Br. J. Ophthalmol.* **89**(5), 529–532 (2005).
8. M. F. Goldberg and A. J. Bron, "Limbal palisades of Vogt," *Trans. Am. Ophthalmol. Soc.* **80**, 155–171 (1982).
9. W. M. Townsend, "The limbal palisades of Vogt," *Trans. Am. Ophthalmol. Soc.* **89**, 721–756 (1991).
10. J. Hong, T. Zheng, J. Xu, S. X. Deng, L. Chen, X. Sun, Q. Le, and Y. Li, "Assessment of limbus and central cornea in patients with keratolimbal allograft transplantation using *in vivo* laser scanning confocal microscopy: an observational study," *Graefes Arch. Clin. Exp. Ophthalmol.* **249**(5), 701–708 (2011).
11. A. Fatima, G. Iftekhar, V. S. Sangwan, and G. K. Vemuganti, "Ocular surface changes in limbal stem cell deficiency caused by chemical injury: a histologic study of excised pannus from recipients of cultured corneal epithelium," *Eye (Lond.)* **22**(9), 1161–1167 (2008).
12. K. M. Hatch and R. Dana, "The Structure and Function of the Limbal Stem Cell and the Disease States Associated With Limbal Stem Cell Deficiency," *Int. Ophthalmol. Clin.* **49**(1), 43–52 (2009).
13. T. Zheng and J. Xu, "Age-related Changes of Human Limbus on *In Vivo* Confocal Microscopy," *Cornea* **27**(7), 782–786 (2008).

14. D. V. Patel, T. Sherwin, and C. N. J. McGhee, "Laser Scanning In Vivo Confocal Microscopy of the Normal Human Corneoscleral Limbus," *Invest. Ophthalmol. Vis. Sci.* **47**(7), 2823–2827 (2006).
15. A. J. Shortt, G. A. Secker, P. M. Munro, P. T. Khaw, S. J. Tuft, and J. T. Daniels, "Characterization of the Limbal Epithelial Stem Cell Niche: Novel Imaging Techniques Permit In Vivo Observation and Targeted Biopsy of limbal Epithelial Stem Cells," *Stem Cells* **25**(6), 1402–1409 (2007).
16. K. Bizheva, N. Hutchings, L. Sorbara, A. A. Moayed, and T. Simpson, "In vivo volumetric imaging of the human corneo-scleral limbus with spectral domain OCT," *Biomed. Opt. Express* **2**(7), 1794–1802 (2011).
17. K. L. Lathrop, D. Gupta, L. Kagemann, J. S. Schuman, and N. Sundarraj, "Optical coherence tomography as a Rapid, Accurate, noncontact method of visualizing the palisades of vogt," *Invest. Ophthalmol. Vis. Sci.* **53**(3), 1381–1387 (2012).
18. K. Grieve, D. Ghoubay, C. Georgeon, O. Thouvenin, N. Bouheraoua, M. Paques, and V. M. Borderie, "Three-dimensional structure of the mammalian limbal stem cell niche," *Exp. Eye Res.* **140**, 75–84 (2015).
19. N. P. Pashtae, N. A. Pozdeyeva, A. A. Voskresenskaya, B. V. Gagloev, and A. A. Shipunov, "Comparative analysis of the value of information provided by anterior segment optical coherence tomography and in vivo confocal microscopy for identifying the palisades of Vogt in normal limbus," *Ann. Ophthalmol.* **1**, 60–68 (2017).
20. M. Haagdoorens, J. Behaegel, J. Rozema, V. Van Gerwen, S. Michiels, S. Ni Dhubghaill, M. J. Tassignon, and N. Zakaria, "A method for quantifying limbal stem cell niches using OCT imaging," *Br. J. Ophthalmol.* **0**, 1–6 (2017).
21. P. Li, L. An, R. Reif, T. T. Shen, M. Johnstone, and R. K. Wang, "In vivo microstructural and microvascular imaging of the human corneo-scleral limbus using optical coherence tomography," *Biomed. Opt. Express* **2**(11), 3109–3118 (2011).
22. K. Bizheva, L. Haines, E. Mason, B. MacLellan, B. Tan, D. Hileeto, and L. Sorbara, "In vivo imaging and morphometry of the human pre-Descemet's layer and endothelium with ultrahigh-resolution optical coherence tomography," *Invest. Ophthalmol. Vis. Sci.* **57**(6), 2782–2787 (2016).
23. K. Bizheva, B. Tan, B. MacLellan, O. Kralj, M. Hajjalamdari, D. Hileeto, and L. Sorbara, "Sub-micrometer axial resolution OCT for in-vivo imaging of the cellular structure of healthy and keratoconic human corneas," *Biomed. Opt. Express* **8**(2), 800–812 (2017).
24. American National Standard for Safe Use of Lasers Z136.1-2007 (2007).
25. A. C. Romano, E. M. Espana, S. H. Yoo, M. T. Budak, J. M. Wolosin, and S. C. Tseng, "Different cell sizes in human limbal and central corneal basal epithelia measured by confocal microscopy and flow cytometry," *Invest. Ophthalmol. Vis. Sci.* **44**(12), 5125–5129 (2003).
26. A. Kumar, W. Drexler, and R. A. Leitgeb, "Subaperture correlation based digital adaptive optics for full field optical coherence tomography," *Opt. Express* **21**(9), 10850–10866 (2013).
27. S. G. Adie, B. W. Graf, A. Ahmad, P. S. Carney, and S. A. Boppart, "Computational adaptive optics for broadband optical interferometric tomography of biological tissue," *Proc. Natl. Acad. Sci. U.S.A.* **109**(19), 7175–7180 (2012).
28. N. D. Shemonski, F. A. South, Y. Z. Liu, S. G. Adie, P. S. Carney, and S. A. Boppart, "Computational high-resolution optical imaging of the living human retina," *Nat. Photonics* **9**(7), 440–443 (2015).
29. L. Yu, B. Rao, J. Zhang, J. Su, Q. Wang, S. Guo, and Z. Chen, "Improved lateral resolution in optical coherence tomography by digital focusing using two-dimensional numerical diffraction method," *Opt. Express* **15**(12), 7634–7641 (2007).
30. A. Kumar, W. Drexler, and R. A. Leitgeb, "Numerical focusing methods for full field OCT: a comparison based on a common signal model," *Opt. Express* **22**(13), 16061–16078 (2014).
31. A. Kumar, T. Kamali, R. Platzer, A. Unterhuber, W. Drexler, and R. A. Leitgeb, "Anisotropic aberration correction using region of interest based digital adaptive optics in Fourier domain OCT," *Biomed. Opt. Express* **6**(4), 1124–1134 (2015).
32. B. Potsaid, I. Gorczynska, V. J. Srinivasan, Y. Chen, J. Jiang, A. Cable, and J. G. Fujimoto, "Ultrahigh speed Spectral / Fourier domain OCT ophthalmic imaging at 70,000 to 312,500 axial scans per second," *Opt. Express* **16**(19), 15149–15169 (2008).
33. L. An, P. Li, T. T. Shen, and R. Wang, "High speed spectral domain optical coherence tomography for retinal imaging at 500,000 A-lines per second," *Biomed. Opt. Express* **2**(10), 2770–2783 (2011).
34. W. Choi, B. Baumann, J. J. Liu, A. C. Clermont, E. P. Feener, J. S. Duker, and J. G. Fujimoto, "Measurement of pulsatile total blood flow in the human and rat retina with ultrahigh speed spectral/Fourier domain OCT," *Biomed. Opt. Express* **3**(5), 1047–1061 (2012).
35. T. Schmoll, C. Kolbitsch, and R. A. Leitgeb, "Ultra-high-speed volumetric tomography of human retinal blood flow," *Opt. Express* **17**(5), 4166–4176 (2009).
36. B. Grajciar, M. Pircher, A. Fercher, and R. Leitgeb, "Parallel Fourier domain optical coherence tomography for in vivo measurement of the human eye," *Opt. Express* **13**(4), 1131–1137 (2005).
37. B. Grajciar, Y. Lehareinger, A. F. Fercher, and R. A. Leitgeb, "High sensitivity phase mapping with parallel Fourier domain optical coherence tomography at 512 000 A-scan/s," *Opt. Express* **18**(21), 21841–21850 (2010).
38. D. Hillmann, H. Spahr, C. Hain, H. Sudkamp, G. Franke, C. Pfäffle, C. Winter, and G. Hüttmann, "Aberration-free volumetric high-speed imaging of in vivo retina," *Sci. Rep.* **6**(1), 35209 (2016).
39. R. Ansari, C. Myrtus, R. Aherrahrou, J. Erdmann, A. Schweikard, and G. Hüttmann, "Ultrahigh-resolution, high-speed spectral domain optical coherence phase microscopy," *Opt. Lett.* **39**(1), 45–47 (2014).

40. H. Sudkamp, P. Koch, H. Spahr, D. Hillmann, G. Franke, M. Münst, F. Reinholz, R. Birngruber, and G. Hüttmann, "In-vivo retinal imaging with off-axis full-field time-domain optical coherence tomography," *Opt. Lett.* **41**(21), 4987–4990 (2016).

1. Introduction

The corneo-scleral limbus is about 1.5 mm wide transitional region of tissue that separates anatomically the peripheral cornea from the conjunctiva. The limbus has a rich and complex morphology [1,2] with dense innervations [3] and vascularization [4,5], that provides an unique environment for housing the corneal epithelial stem cells [6,7]. The limbus contains radially oriented fibro vascular ridges, known as the palisades of Vogt (POV), that are interspaced by epithelial rete ridges or so called limbal epithelial crypts [8,9]. The structure of the POV is as unique as fingerprints, and their shape, size and spatial distribution vary over time with age, as well as in response to medication, surgery or congenital conditions [10–13]. The limbal epithelial crypts house stem cells, which play a key role in the regeneration of the corneal epithelium [6,7]. The limbus also provides a "barrier" between the corneal epithelium and the conjunctiva that prevents proliferation of conjunctival cells into the corneal epithelium [6]. The scleral part of the limbus contains both a rich vascular network responsible for oxygen and nutritional supply of the peripheral cornea, and a complex aqueous outflow system (Schlemm's canal, trabecular meshwork), responsible for the aqueous humor circulation and waste management [4,5,8].

A number of optical imaging techniques have been used to examine the limbal morphology and vasculature both *ex-vivo* and *in-vivo*. Slit-lamps [8] offer an in-expensive, non-contact method for clinical imaging of the limbus, however, this method can only visualize the surface of the POV and the spatial resolution is not sufficient for imaging and identification of individual limbal epithelial cells. Cellular level resolution images of the human corneo-scleral limbus that are acquired *in-vivo* with commercial laser scanning confocal microscopes (LSCM), show detailed enface view of the POV and the limbal epithelial crypts [13–15]. Although the quality of these images is impressive, there are a few limitations to using LSCM for corneal and limbal imaging: a) the measurement procedure requires physical contact between the imaging probe and the corneal epithelium or conjunctiva, which can cause patient discomfort and increase the risk of tissue abrasions and inflammation; b) since the LSCM field of view is relatively small (~400 μm x 400 μm), a 2D view of ~1 mm x 1 mm area of the corneo-scleral limbus requires acquisition and "stitching" of multiple LSCM images, thus increasing significantly the image acquisition and processing time; and c) due to the limited LSCM axial resolution, volumetric visualization of the limbal morphology is not trivial.

Optical coherence tomography (OCT) offers the advantages of non-contact, high resolution, volumetric imaging of both the limbal structure and vasculature. Bizheva [16] published the first *in-vivo*, high resolution OCT images of the healthy human limbus that showed the termination of the Bowman's membrane, nerve fiber bundles, limbal microvasculature, the POV and the Schlemm's canal. However, the limited axial and lateral resolution (3 μm and ~18 μm respectively) prevented visualization of individual limbal epithelial cells at that time. Lathrop [17] conducted an *ex-vivo* comparative study on healthy limbal tissue using confocal microscopy and a research grade OCT system that offered 3.5 μm axial and ~20 μm lateral resolution. That study generated surface maps of the POV from the OCT images; however, the cellular structure of the limbal tissue was not resolved due to the low spatial OCT resolution. Grieve [18] utilized Full-Field OCT (FF-OCT) that offers ~1 μm isotropic resolution to image the cellular structure and analyze morphometrically the limbal crypts *ex-vivo* in animal and human limbal tissue. By combining FF-OCT with fluorescence confocal microscopy, Grieve and her colleagues were able to identify limbal stem cells. More recently, Pashtaev [19] used commercial OCT (RTVue XR Avanti) and *in-vivo* confocal microscopy (IVCM) to generate and compare enface images of the healthy superior and inferior human limbus. Haagdorens [20] also used a commercial OCT (RTVue

100–2) to image the POV in healthy subjects and to visualize the loop-like appearance of the POV folds in cross-sectional images acquired *in-vivo* from healthy subjects. In both cases, the spatial resolution of the commercial OCT devices was not sufficient to visualize the cellular structure of the limbus. Li [21] utilized anterior segment OCT integrated with optical microangiography (OMAG) to image *in-vivo* the vasculature of the healthy human limbus.

Here we present for the first time, cross-sectional and volumetric OCT images of the cellular structure of the limbal crypts and the POV, that were acquired *in-vivo* from healthy human subjects without contact between the OCT imaging probe and the limbal tissue. Furthermore, the high spatial OCT resolution allowed for visualization of the capillaries that extend from the inside of the palisades' ridges to a lateral micro-vascular network located underneath the POV.

2. Methods

2.1 OCT system design

A sub-micrometer axial resolution OCT system was developed recently by our research group for *in-vivo*, cellular resolution imaging of the healthy and pathological human cornea [22,23]. The same OCT system was used in this study to image the cellular structure of the healthy human limbus. Briefly, the system is based on a fiberoptic, spectral domain OCT design and operates in the 800 nm spectral range. It utilizes a broadband supercontinuum laser (SuperK; NKT Photonics, Birkerød, Denmark), a custom filter to select about ~380 nm wide spectral region centered at ~800 nm with ~250 nm FWHM, and to reduce the optical power to a level safe for *in-vivo* ocular imaging, a customized commercial spectrometer (Cobra; Wasatch Photonics, Durham, NC, USA), and an infrared enhanced camera (Piranha NH-80-08K40; Teledyne Dalsa, Canada), in order to achieve ~0.95 μm axial resolution in biological tissue at 34,000 A-scan/s image acquisition rate. The OCT system's SNR was ~95 dB near the zero delay line for ~700 μW optical power of the imaging beam incident on the limbal tissue. Although the camera is based on an 8192 pixel linear array, the spectrometer was designed to illuminate only 4600 pixels to limit signal loss at the array periphery associated with optical aberrations. Due to the very broad spectrum and the limited size and number of illuminated camera pixels, the SNR roll-off in free space was ~10 dB over a range of 1.2 mm. The OCT imaging probe was designed to interface easily with microscope objectives of different magnification. In this study, 5x and 10x objectives were used to achieve ~4 μm and ~2 μm lateral resolution in biological tissue with field-of-view (FOV) of about 2 mm x 2 mm and 1 mm x 1 mm respectively. To ensure safety of the imaged subjects, the optical power of the imaging beam incident on the tissue surface was limited to ~700 μW , which is below the maximum permissible exposure as specified by the American National Standards Institute (ANSI) [24].

2.2 Imaging procedure and histology

This study was approved by the Research Ethics Committee at the University of Waterloo and was carried out in compliance with the tenets of the Declaration of Helsinki. OCT images of the corneo-scleral limbus were acquired from 10 healthy participants aged 21 to 60. All subjects passed a slit-lamp biomicroscopy screening and provided written consent for participation in the study.

Volumetric OCT images (1000 A-scans x 256 B-scans x 2300 pixels) were acquired from both eyes in a radial direction from the nasal limbus and tangential direction from the inferior limbus with both the 5x and 10x microscope objectives. The B-scan rate was 34 fps, while the image acquisition time for a 3D imaging stack was 7.5 seconds. The size of the imaged area was 2 mm x 0.5 mm with the 5x objective and 1 mm x 0.25 mm with the 10x objective, which corresponds to ~2x oversampling of the data in the X and Y directions. The OCT images were generated from the raw data and then numerically dispersion compensated up to

the 9th order with custom Matlab (Mathworks, USA) based algorithms. Both an automatic algorithm and manual alignment of the B-scans were used to generate volumetric OCT images of the human limbus.

In order to compare the OCT images with histology, human cadaver tissue was used. Consecutive sections of the normal human ocular globes were processed for microscopic analysis following the procedure: after initial fixation in 10% neutral buffered formalin, the tissue was embedded in paraffin, serially sectioned in 5 μm thick sections, and stained with hematoxylin and eosin (H&E). The histological slides were evaluated using bright field microscopy (Leica DM1000, ICC50 HD, Leica Microsystems Inc, Canada) and optical images were acquired at different magnifications to visualize the cellular structure of the limbal crypts, the POV and the limbal microvasculature. The histological images were acquired from locations of the nasal and inferior limbus very similar to the ones used for the *in-vivo* OCT imaging procedure.

3. Results

Figure 1 shows cross-sectional OCT images of the healthy human inferior limbus acquired *in-vivo*, in the tangential direction with the 5x microscope objective, closer to the corneal end of the limbus (A) and closer to the scleral end of the limbus (B). The POV appear as highly reflective, narrow, loop-like structures in Fig. 1(A), while closer to the sclera (Fig. 1(B)), their height diminishes and they appear as small reflective bumps. Blood vessels (V) appear as dark shadows on the highly scattering background of the scleral connective tissue. Capillaries appear to extend from the inside of the fibrous folds of the POV in a vertical direction and connect with a lateral vascular network located $\sim 20\ \mu\text{m}$ to $50\ \mu\text{m}$ below the base of the POV

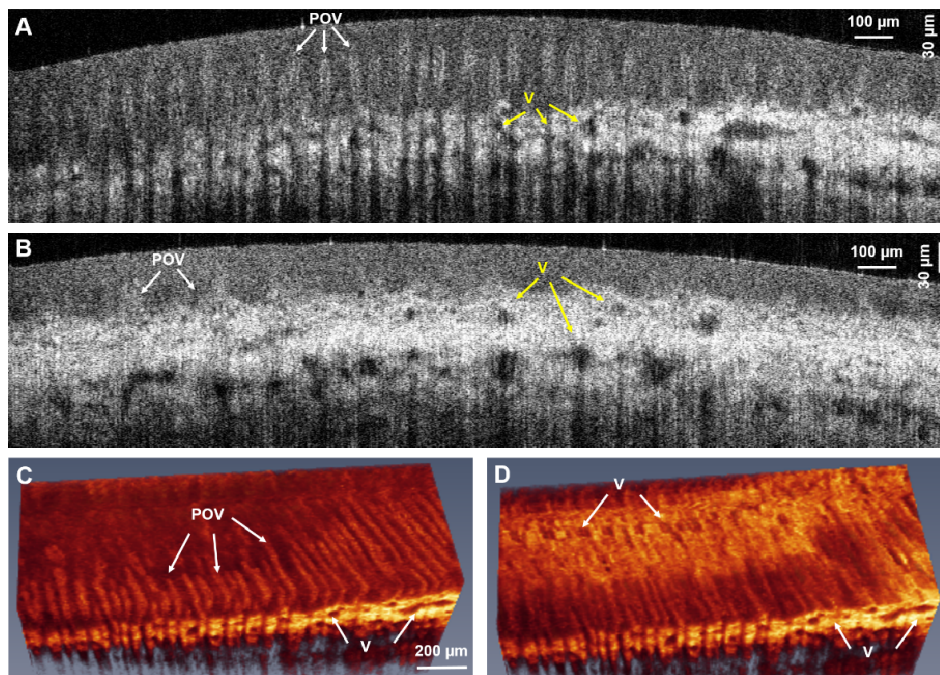


Fig. 1. Cross-sectional OCT images of the healthy human inferior limbus acquired *in-vivo*, in a tangential direction with the 5x microscope objective, closer to the corneal end of the limbus (A) and closer to the scleral end of the limbus (B). The POV appear as highly reflective, narrow, loop-like structures in Fig. 1(A). Blood and lymph vessels (V) appear as dark shadows on the highly scattering background of the collagen matrix. Capillaries extend from the inside of the fibrous sacks of the POV in vertical direction and connect with a lateral vessels network located $\sim 20\ \mu\text{m}$ to $50\ \mu\text{m}$ below the base of the POV. Volumetric images of the inferior limbus (C, D).

(Fig. 1(A)). A volumetric image of the inferior POV is presented in Fig. 1(C), where the top edge of the image corresponds to the peripheral cornea. The POV appear in this image as finger-like structures of various lengths and the lateral vascular network (V) is clearly visible on the side view of the volumetric image stack. A different C-scan of the image stack, generated by maximum intensity projection and located at a depth of $\sim 70 \mu\text{m}$ below the limbal tissue surface, is shown in Fig. 1(D). It reveals the microvasculature on the corneal side of the limbus that is composed of both vessels that extend vertically and therefore have approximately circular cross-sections in the image, and vessels that run laterally and therefore appear as dark lines on the highly scattering background of the connective tissue matrix.

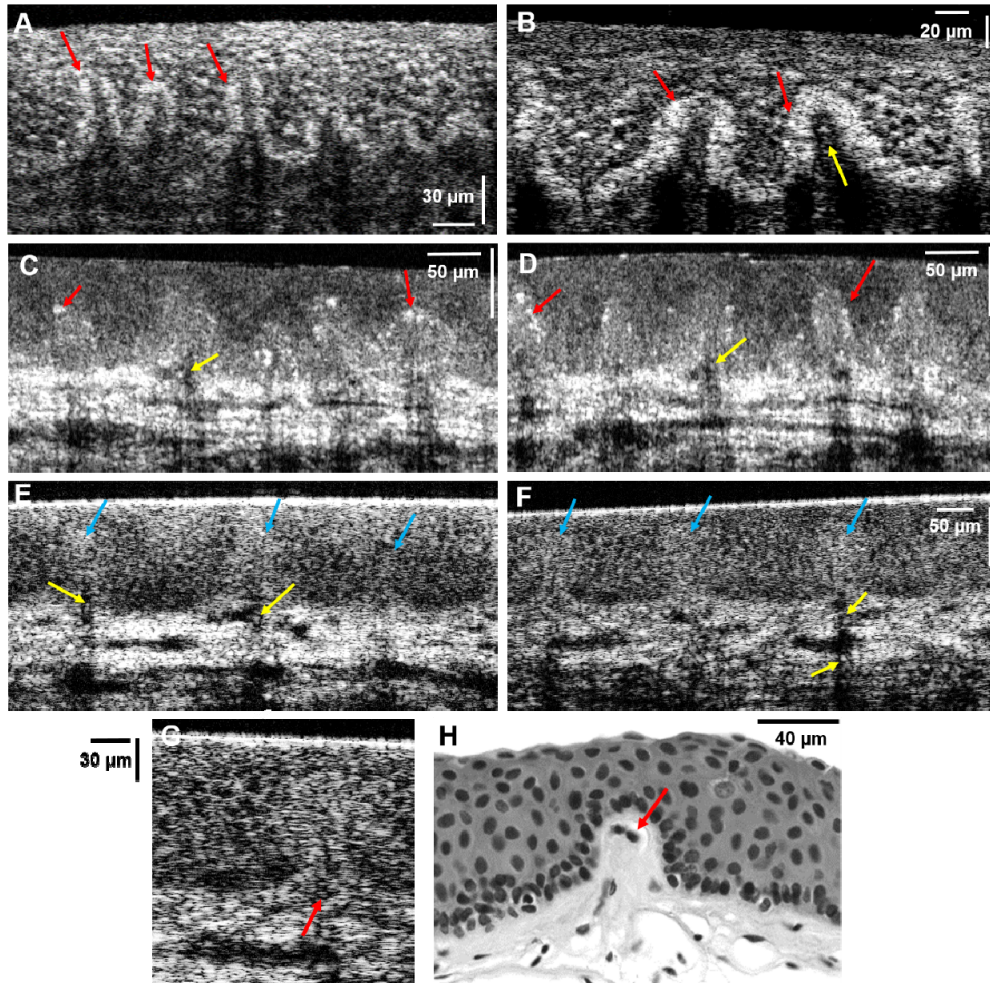


Fig. 2. Cross-sectional OCT images of the healthy human inferior limbus acquired *in-vivo* in a tangential direction with the 10x microscope objective from subjects with highly pigmented (A, B), moderately pigmented (C, D) and mildly pigmented (E, F) palisades of Vogt. The POV appear as loop-like structures with reflective envelope (red arrows). The cellular structure of the crypts, located between the POV is clearly visible. Yellow arrows mark hyper-reflective dots inside the vasculature that most likely correspond to individual red blood cells in the capillaries extending from the inside of the POV to a lateral vascular grid in the connective tissue underneath. A magnified view of a single POV acquired with the OCT system (G) and compared to histology from cadaver limbal tissue (H). Red arrows in both G and H mark red blood cells.

Higher magnification cross-sectional OCT images of the inferior limbus acquired in a tangential direction with the 10x microscope objective from 3 subjects with different pigmentation level of the POV are shown in Fig. 2 (A and B - highly pigmented subject; C and D - subject with moderate pigmentation; E and F – mildly pigmented subject). In all of the images, the POV appear as loop-like structures with a reflective envelope that corresponds to the fibrous connective tissue of the palisades' ridges. Red arrows in Fig. 2(A)-2(D) mark highly reflective (white) spots that most likely correspond to pigmented cells, containing larger amounts of melanin that tend to line up along the outer surface of the POV. Such hyper-reflective spots are not observed in the images acquired from the subject with mildly pigmented POV (Fig. 2(E)-2(F)) and the fibrous loops of the POV are marked with blue arrows. The cellular structure of the limbal crypts, located between the POV is visible, especially in the images acquired from the subject with mildly-pigmented POV. The images also reveal capillaries that extend in a vertical direction from the inside of the loops of the POV and connect with a lateral network of micro-vessels located in the connective tissue directly underneath the POV. The hyper-reflective spots visible inside the capillaries and marked with yellow arrows in the images in Fig. 2(A)-2(F) most likely correspond to red blood cells. These reflective spots persisted even when OCT images are processed with speckle denoising algorithms, which suggests that they correspond to real morphological features instead of speckle. Figures 2(G) and 2(H) show OCT and H&E stained histology images respectively, of a single POV loop from non-pigmented subjects. The red arrows mark individual red blood cells in both images.

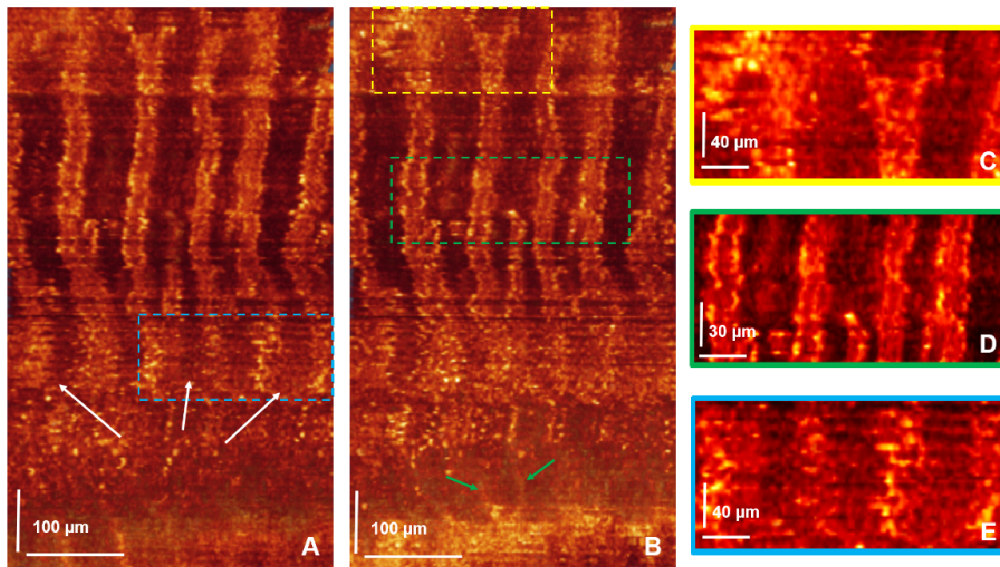


Fig. 3. Enface images of the POV (A and B) generated by maximum intensity projection from a volumetric image stack acquired in tangential direction from the inferior limbus with the 10x objective. The image in 3B corresponds to a depth location of $\sim 20 \mu\text{m}$ underneath the image shown in 3A. The white arrows in 3A mark “channel-like” morphological features with distinct cellular structure that extend from the limbal epithelial crypts toward the peripheral cornea. The green arrows in 3B mark blood microvasculature in the peripheral cornea that appears as this reflective (yellow) lines extending in radial direction. Figures 3(C)-3(E) show magnified views of the regions in 3A and 3B marked with the colored rectangles. The cellular structure of the limbal crypts is visible in the magnified images.

Figures 3(A) and 3(B) show enface images of the POV generated by maximum intensity projection from the rendered volumetric OCT image stack that was acquired in a tangential direction from the inferior limbus with the 10x magnification objective. The enface images correspond to two different depths, separated by $\sim 20 \mu\text{m}$. The upper edge of the enface

images corresponds to the scleral end of the limbus, while the lower edge corresponds to the corneal end of the limbus. The POV appear as long, finger-like structures with varying length, width and shape. Hyper-reflective (yellow) dots located along the outer surface of the POV most likely correspond to pigmented cells. The cellular structure of the limbal crypts located between the POV can be observed more clearly in Figs. 3(C) and 3(D) that show magnified views of the regions in Fig. 3(B) marked with the yellow and green rectangles. The fibrous connective tissue of the POV appears more reflective in those images. The base of the limbal crypts opens up to what appear as channel-like structures with a very distinct cellular structure that extend toward the periphery of the cornea (region in Fig. 3(A) marked with blue rectangle and white arrows; magnified view is presented in Fig. 3(E)). Since the image in Fig. 3(B) was generated from a deeper location in the limbus, small capillaries that appear as thin reflective (yellow) lines are observed near the peripheral cornea (marked with green arrows).

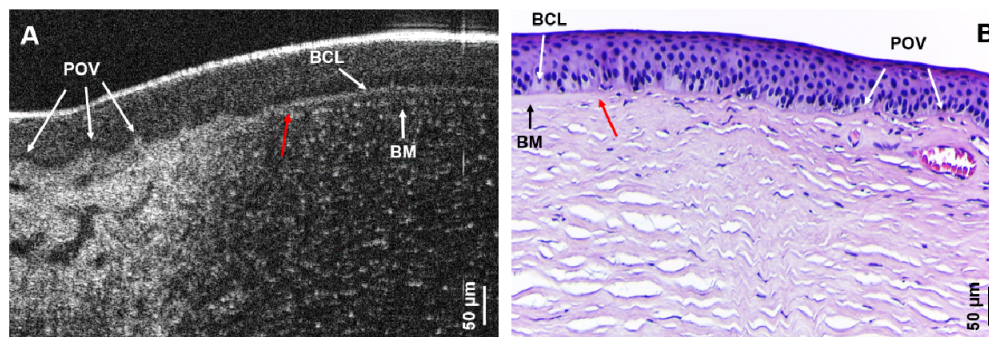


Fig. 4. Cross-sectional OCT image of the healthy nasal human limbus acquired in radial direction with the 5x microscope objective (A) and a corresponding H&E stained histological cross-section (B). BCL – basal cell layer of the corneal epithelium, BM – Bowman's membrane, POV – palisades of Vogt. The red arrow marks the termination of the BM at the limbus.

Figure 4(A) shows a representative cross-sectional OCT image of the healthy human limbus acquired in a radial direction from the nasal limbus with the 5x microscope objective, while a typical histological image of the same region is presented in Fig. 4(B). The high axial OCT resolution allowed for clear visualization of the epithelial basal cell layer (BCL), which appears as the most posterior, dark, low reflective layer of the epithelium in the peripheral cornea and the limbus. However, the limited lateral resolution of the 5x objective ($\sim 4 \mu\text{m}$) prevented visualization of individual basal cells. Bowman's membrane (BM) is clearly visible in the corneal side of the OCT image and its termination at the limbus is marked with a red arrow. The POV appear as highly reflective peaks of various sizes, protruding into the limbal epithelium. The same morphological features are clearly identified in the histological image (Fig. 4(B)). The POVs appear in the histology images as small "hills" of connective tissue protruding in vertical direction from the sclera toward the limbal epithelium. The BM appears in the upper left corner of the histology image as a very thin, smooth layer located between the basal cell layer of the corneal epithelium and the most anterior boundary of the corneal stroma. The termination of the BM at the limbus is marked with a red arrow in Fig. 4(B).

Representative cross-sectional images of the nasal limbus acquired in a radial direction with the 10x microscope objective are shown in Fig. 5(A) and 5(C). Selected regions of the epithelial layer in Figs. 5(A) and 5(C) (marked with dashed yellow line) were magnified and presented in Figs. 5(B) and 5(D)-5(F) to show a closer look at the individual limbal cells. The white arrow in Fig. 5(A) marks the interface between the limbal epithelium and the conjunctiva. The conjunctiva appears more optically scattering in the OCT images, most likely because it has a different cellular structure [25]. The underlying scleral tissue appears highly reflective as it is largely composed of a collagen. The larger, dark morphological

features in the sclera correspond to the limbal vascular network. The high OCT resolution also allowed for clear visualization of a number of morphological features in the limbus that are typically not observed in lower resolution OCT images. For example, the small, hyper-reflective dots inside the blood vessels in Figs. 5(A) and 5(C) marked with the yellow arrows most likely correspond to reflections from individual or clusters of red blood cells. Figures 5(B) and 5(D)-5(F) show individual cells in the limbal epithelium. Hyper-reflective dots inside the cells (marked with red arrows) most likely correspond to reflections from the cellular nuclei, given the larger refractive index of the nuclei relative to the cytoplasm. The green arrows mark reflective spots in the BCL of the limbal epithelium that most likely correspond to pigmented epithelial cells. Figures 5(D) and 5(E) show radial cross-sections of 2 POV of different heights. The blue arrows in Figs. 5(A), 5(C) and 5(D) mark the tear film.

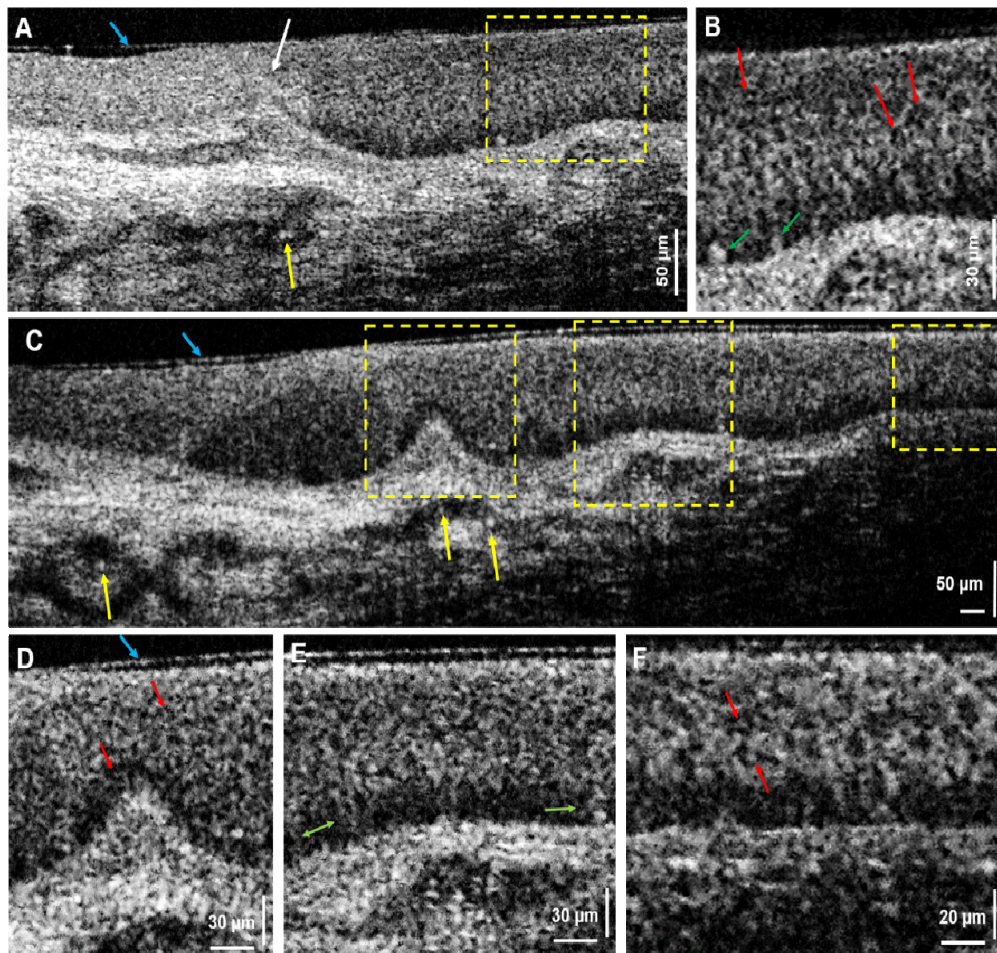


Fig. 5. Cross-sectional OCT images of the healthy human nasal limbus acquired *in-vivo*, in a radial direction with the 10x microscope objective (A and C). 2x magnified versions of the regions in Fig. 5(A) and Fig. 5(C) marked with the yellow dashed lines (Fig. 5(B), 5(D)-5(F)). Green arrows mark reflections from pigmented epithelial cells, red arrows mark reflections from nuclei in the limbal epithelial cells, yellow arrows mark reflection from red blood cells in the limbal vasculature, blue arrows mark the tear film and the white arrow marks the boundary between the conjunctiva and the limbal epithelium.

4. Discussion

The high spatial resolution provided by the sub-micrometer axial resolution OCT system is sufficient to observe the cellular structure of the limbal epithelial crypts and the limbal microvasculature both in cross-sectional and volumetric images. Although the limbal images generated in this study are of very similar quality to the ones acquired *ex-vivo* with the FF-OCT [18], the images of the limbal epithelial cells are not as sharp as the ones generated by IVCM. There are two major factors that cause the blur and partial loss of contrast in the OCT images of the limbal epithelial cells generated in our study. One: the propagation of a focused optical beam through a biological medium that is characterized with a heterogeneous refractive index, introduces various optical aberrations. The IVCM imaging probes are specifically designed to minimize some of these aberrations through either direct physical contact with the imaged tissue, or through a water based gel placed on the tissue surface, and thus partially matching the average refractive index of the biological tissue with the one of the imaging lens. Furthermore, IVCM instruments utilize light sources with very narrow spectral bandwidths that minimize chromatic aberrations. In contrast, the OCT limbal images presented here were acquired without contact of the OCT imaging probe with the limbal tissue. Furthermore, the OCT system used in this study requires a light source with very broad spectral bandwidth (~ 380 nm at 10 dB and ~ 250 nm at 3 dB), in order to generate axial resolution < 1 μm , which results in significant chromatic aberrations that affect both the axial and lateral OCT resolution. Optical aberrations can be compensated partially by use of computational adaptive optics (CAO). Over the past decade a number of different CAO approaches have been proposed to compensate for optical aberrations in OCT images [26–31]. One common element to all of these approaches is the requirement for high phase stability of the OCT data, which necessitates OCT image acquisition rates $> 2,500$ B-scans /s in the case of *in-vivo* imaging of biological tissue.

The second factor that affects the OCT image quality is the image acquisition rate relative to the speed of ocular micro-saccades. The current design of the OCT system utilizes a camera with a rate of 34,000 A-scans/s that is too slow compared to the speed of typical saccades in the eye. This causes partial washout of the OCT spectral fringes and results in loss of axial resolution and image contrast, as well as introduces significant motion artefacts in the volumetric images. Such axial motion artefacts appear as dark and bright lines in the images in Fig. 3 even after very careful manual alignment of the OCT B-scans. CMOS cameras with 4096 pixel linear arrays and data acquisition rates of up to 140 kHz are commercially available and have been utilized in the past to achieve OCT image acquisition rates of up to 500,000 A-scans/s [32–35] that resulted in OCT images with fewer motion artefacts. However, the higher image acquisition rates in those cases were achieved by reducing the number of read-out camera pixels, which resulted in significant loss of OCT axial resolution and SNR, as well as shorter OCT scanning range. Future development of Si-based cameras that can combine both high imaging speed with large number of pixels (8192) with tall pixel design would improve significantly the quality of the images acquired with the sub-micrometer axial resolution OCT technology described here. Alternative approaches to high speed OCT imaging that would allow for effective use of CAO to improve the image quality, include line scan OCT (LS-OCT) [36–37] and FF-OCT [38–40]. Both of these OCT designs require ultra-high speed cameras that are very expensive, as well as trade-in of lateral resolution in X or Y direction (LS-OCT) or depth of focus (FF-OCT) to achieve the high image acquisition rates required for successful application of CAO.

The OCT limbal images acquired from the 10 healthy subjects in our pilot study showed that the dimensions and shape of the POV are spatially dependent and unique for each subject, which agrees well with conclusions from other studies that employed different imaging modalities such as IVCM and slit lamps to image the POV. Furthermore, OCT images of the limbus acquired from Caucasian subjects with blue, green and grey color of the iris showed presence of very few and sparsely located pigmented cells in the limbal crypts

(Fig. 2(E)-2(F)). Subjects with Middle Eastern and Asian origin and brown pigmentation of the iris showed significantly larger number of pigmented cells in the limbal crypts (Fig. 2(C)-2(D)). Only one of the 10 subjects in the study (Middle Eastern origin and brown iris color) showed excessive pigmentation of POV (Fig. 2(A)-2(B)). Although these results may suggest a relationship between the subject's origin and iris color and the number of pigmented cells in the limbus, no definitive conclusion can be drawn regarding such a link at this time given the very limited number of subjects in our pilot study.

Limbal stem cell dysfunction or dystrophy (LSCD) causes both morphological and physiological changes in the limbus that result in decreased vision, photophobia, tearing, chronic inflammation and hyperemia, recurrent episodes of pain, and blindness in severe cases. LSCD can be treated both medically (topical medications and therapeutic contact lenses) and surgically (transplantation of healthy stem cells). Currently, there is no clinical imaging modality that can image the cellular structure of the limbal crypts and identify limbal stem cells (LSC) without direct or indirect contact of the imaging probe with the limbal tissue. Ultra-high resolution optical coherence tomography (UHR-OCT) allows for non-contact, volumetric cellular resolution imaging of the limbus that may be able to assist surgeons with mapping out and correctly identifying healthy LSC zones from LSC-deficient areas. Although currently UHR-OCT cannot identify LSC from the rest of the cell types present in the limbal crypts, upgrading the UHR-OCT system with a fluorescence channel and use of fluorescent dyes developed specifically for labeling LSC can make such an identification possible. This will permit safe targeted harvesting of donor LSC and accurate placement of LSC transplants in areas of deficiency. Therefore, a combined UHR-OCT + Fluorescence system could become a valuable clinical tool for LSCD diagnosis and grading, monitoring the treatment of LSC deficiency, as well as pre-operative planning.

5. Conclusions

In conclusion, we demonstrated that sub-micrometer axial resolution OCT is able to visualize the cellular structure of the limbal crypts and the micro-vasculature of the healthy human limbus in 3D and without contact of the OCT imaging probe with the limbal tissue. Future improvements of the OCT system's image acquisition rate by employing a faster camera, would reduce significantly the presence of motion artefacts in the OCT images. By combining the UHR-OCT technology with fluorescence imaging, *in-vivo* identification of LSC in the limbal crypts would become feasible. Ultra-high resolution OCT could provide a safe, non-contact method for diagnosing limbal stem cell deficiency (LSCD) and monitoring its treatment, and an alternative approach to excisional biopsy in limbal tumors suspicious for ocular surface squamous neoplasia.

Funding

This study was funded in part by the Canadian Institutes of Health Research (CIHR) (446387), the Natural Sciences and Engineering Research Council of Canada (NSERC) (312037 and 446387) and University of Waterloo start up fund (D. Hileeto).

Disclosures

The authors declare that there are no conflicts of interest related to this article.